nature neuroscience

SUPPLEMENTARY INFORMATION

https://doi.org/10.1038/s41593-018-0189-y

In the format provided by the authors and unedited.

Principles governing the integration of landmark and self-motion cues in entorhinal cortical codes for navigation

Malcolm G. Campbell[1]*, Samuel A. Ocko[2,3], Caitlin S. Mallory[1,3], Isabel I. C. Low[1], Surya Ganguli[1,2] and Lisa M. Giocomo[1]*

[1]Department of Neurobiology, Stanford University School of Medicine, Stanford, CA, USA. [2]Department of Applied Physics, Stanford University, Stanford, CA, USA. [3]These authors contributed equally:Samuel A. Ocko, Caitlin S. Mallory. *e-mail: malcolmc@stanford.edu; giocomo@stanford.edu

m1: 16 grid, 4 border, 10 speed

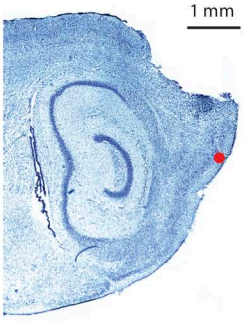

m2: 5 grid, 5 border, 6 speed

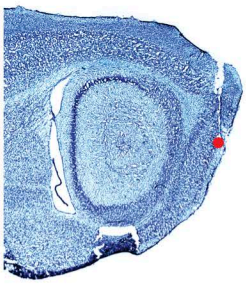

m3: 1 grid, 8 border, 12 speed

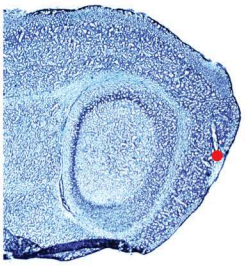

m4: 2 grid, 12 border, 12 speed

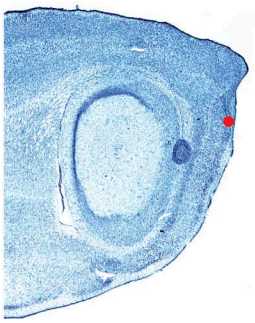

m6: 5 grid, 4 border, 11 speed

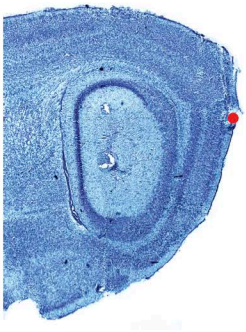

m7: 0 grid, 4 border, 6 speed

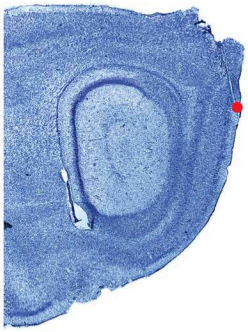

m8: 7 grid, 4 border, 7 speed

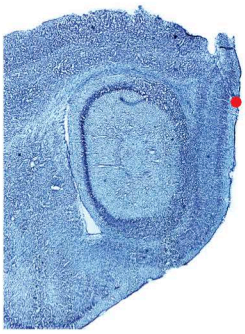

m10: 1 grid, 4 border, 4 speed

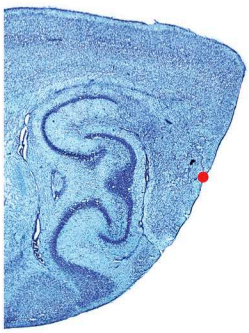

m11: 1 grid, 1 border, 3 speed

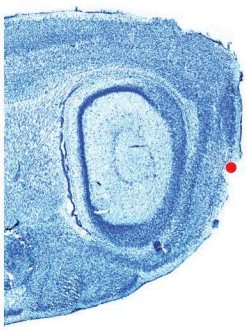

m12: 1 grid, 6 border, 9 speed

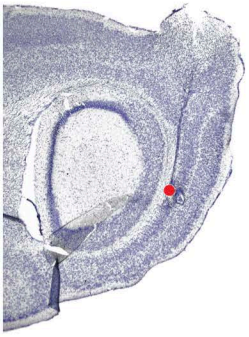

m13: 4 grid, 20 border, 6 speed

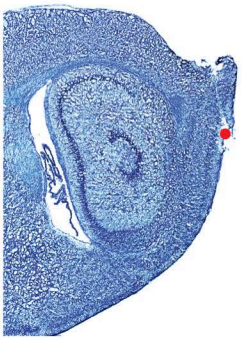

m14: 1 grid, 1 border, 1 speed

m15: 8 grid, 1 border, 8 speed

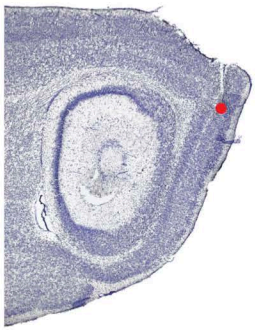

m16: 6 grid, 2 border, 12 speed

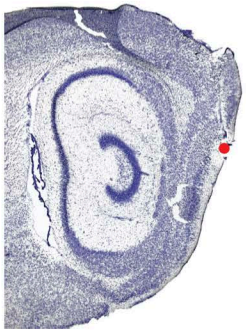

m18: 4 grid, 1 border, 7 speed

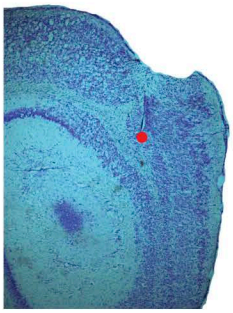

m20: 2 grid, 3 border, 2 speed

m21: 6 grid (Figure 6 only)

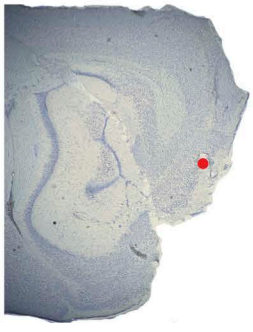

Supplementary Fig. 1: Histology for 17 out of 21 mice. Red dots indicate the location of the end of the tetrode track. There was some damage to m1 during brain extraction, but the tetrode track was still visible within the MEC. Histology was not obtained for four mice due to damage to the brain during extraction. In those mice, identical coordinates were used and classical MEC cells (e.g. grid cells) were recorded, indicating tetrode placement in the MEC. The number of functionally-defined neurons from each animal that were included in the paper (i.e., recorded in both open field and VR) is listed at the top of each image. Six grid cells from m21 were included in Figure 6 and no data from this mouse were used anywhere else in the paper. Numbers of cells in each group for the four mice without histology: m5, 4 grid, 11 border, 6 speed; m9, 4 grid, 4 border, 4 speed; m17, 2 grid, 0 border, 0 speed; m19, 22 grid, 2 border, 8 speed.

Supplementary Fig. 2

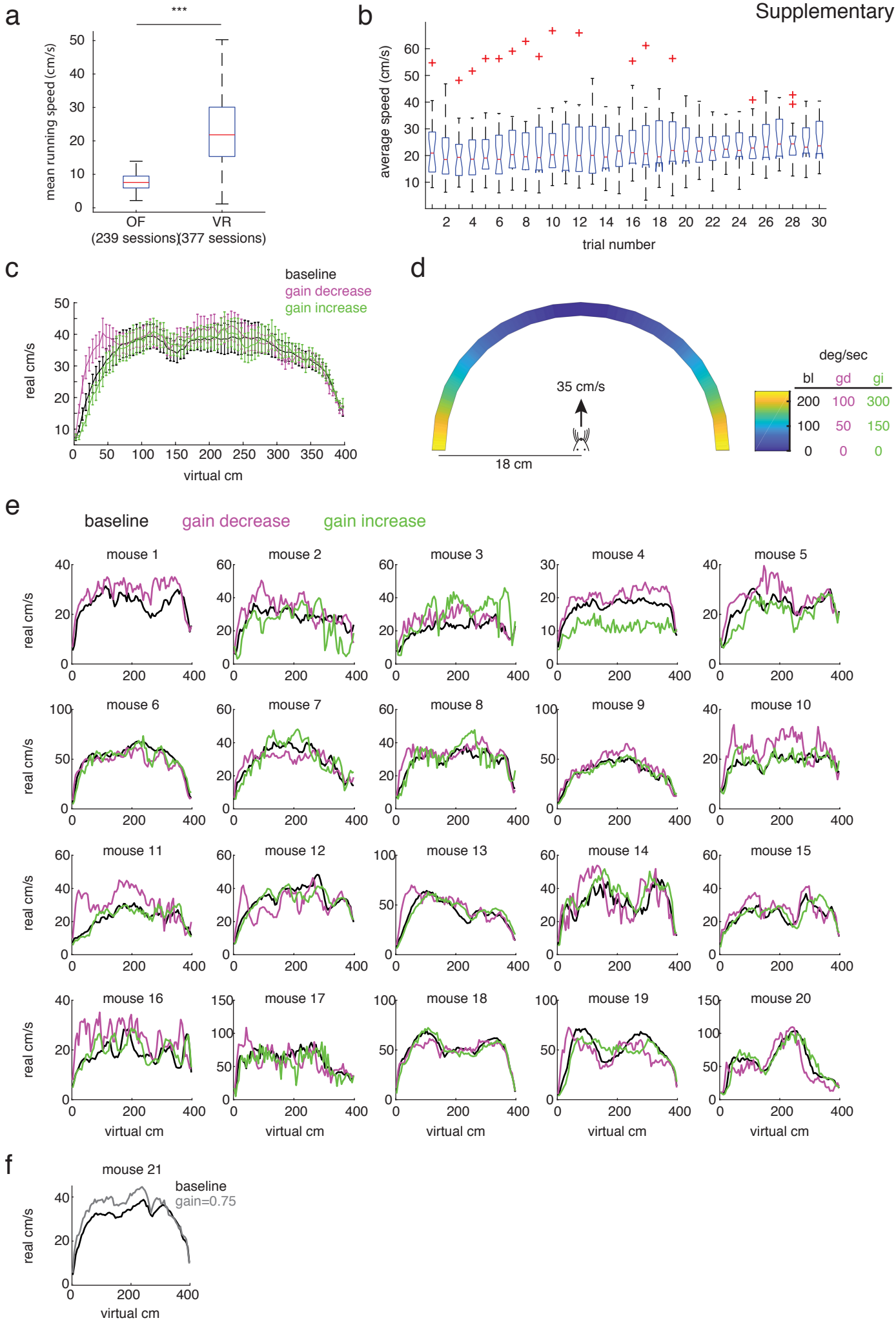

Supplementary Fig. 2: Mouse behavior in VR. **a)** Mean running speeds were higher in VR compared to open field (OF) (median average speed ± SEM: OF = 7.6 ± 0.2 cm/s, n = 239 sessions, VR = 21.8 ± 0.5 cm/s, n = 377 sessions, Wilcoxon rank-sum $p < 1e\text{-}68$). In box plots, the red line is the median, edges of the box are the 25th and 75th percentiles, and the whiskers extend to the extremes of the distribution. **b)** Running speeds did not change over trials, indicating that drift observed in grid cells was not due to changing running speeds over time (ANOVA $p = 0.999$, n = 20 mice averaged over first 30 trials of all sessions). Boxplots as in (a), except that notches display 95% confidence intervals of medians, whiskers extend to the most extreme non-outlier data points, and outliers are plotted individually. **c)** Average running speed with respect to virtual location on the track. In gain manipulation sessions, mice ran at similar speeds and continued to slow down at the same location. Lines: mean running speed ± SEM over mice (n = 20). **d)** Angular velocity of visual cues as a function of position on the hemispherical screen when the mouse is running at 35 cm/s. During gain decreases (gd) and gain increases (gi), these values were multiplied by 0.5 or 1.5, respectively. Even during gain increases, angular velocities were well within the range that optimally drove neurons in visual cortex[40], indicating that visual speed was still within the perceptual range of the mouse. **e)** Average running speed vs. track location for each mouse individually. Black: baseline, pink: gain decrease, green: gain increase. **f)** Average running speed for m21 during baseline (black) and gain=0.75 (gray) trials.

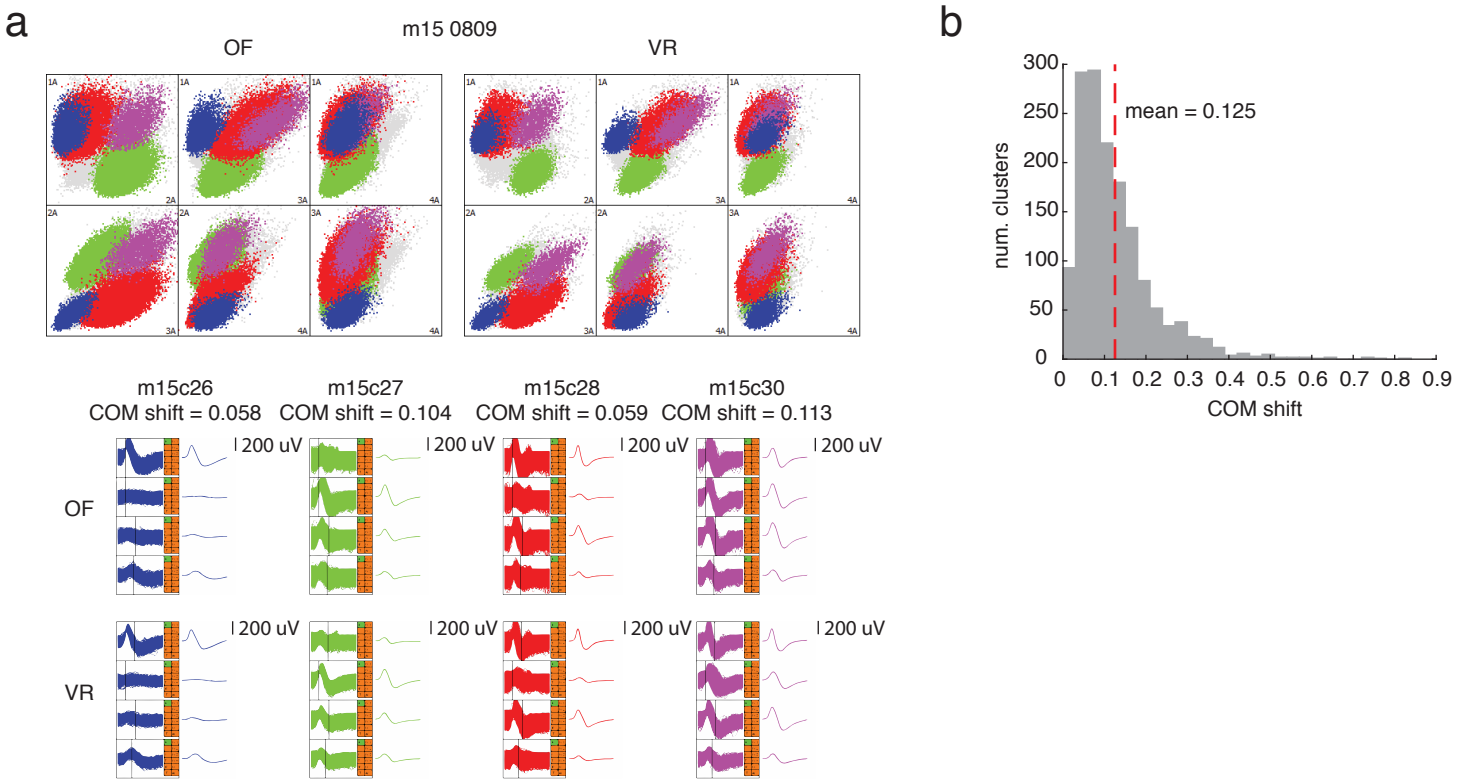

Supplementary Fig. 3: Cluster matching between open field (OF) and VR. **a)** Top: Example clusters in OF and VR. Bottom: Mean waveform for each cluster in OF and VR. Clusters are labeled with their cell ID (mxcy refers to mouse x cell y). COM: Center-of-mass. **b)** Distribution of cluster COM shifts between OF and VR for all cells identified in both environments. Dotted line indicates mean (0.125, n = 1514 pairs of clusters).

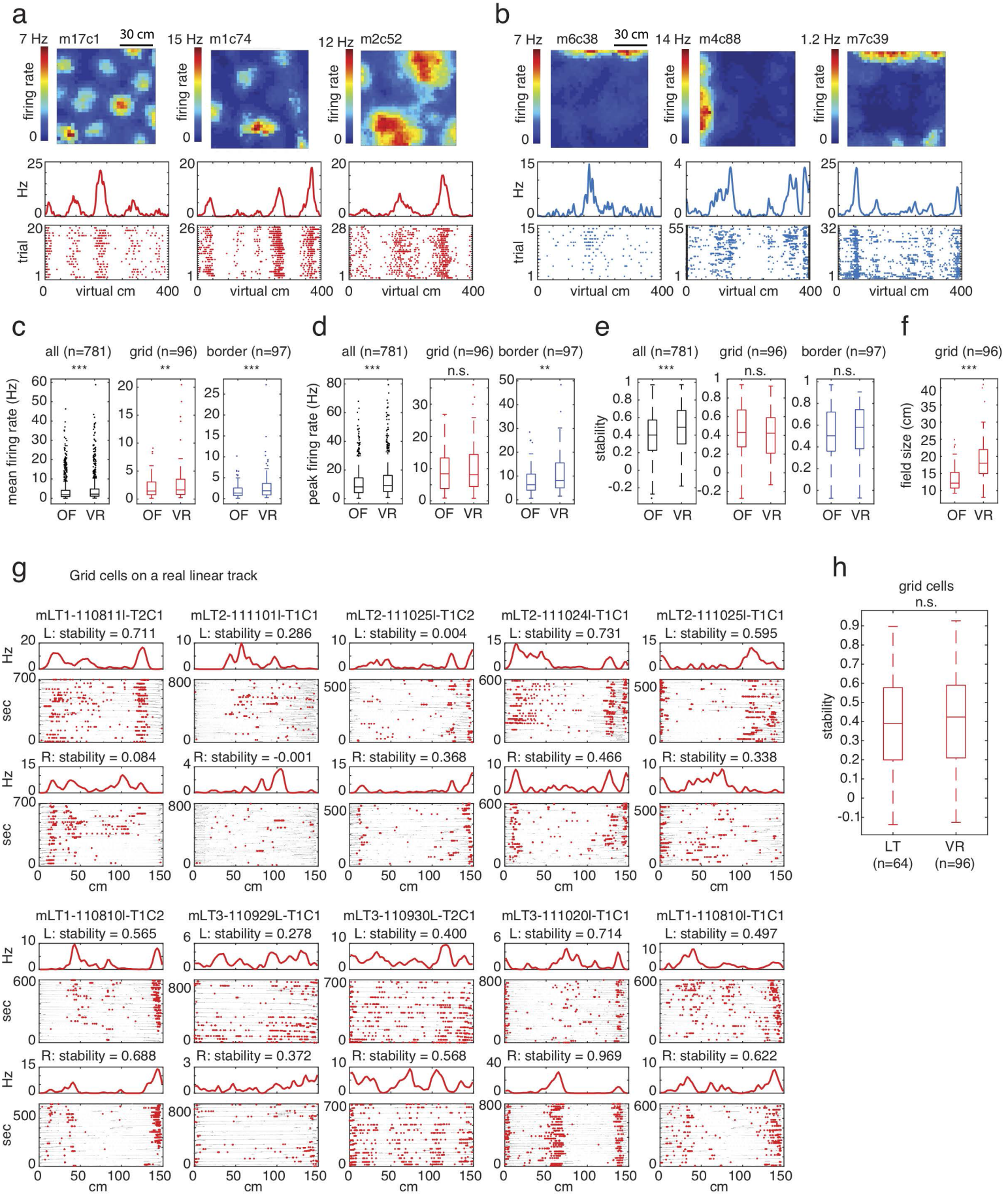
a
7 Hz m17c1
30 cm
15 Hz m1c74
12 Hz m2c52
firing rate
Hz
trial
virtual cm
b
7 Hz m6c38
14 Hz m4c88
1.2 Hz m7c39
c
all (n=781)
grid (n=96)
border (n=97)
mean firing rate (Hz)
OF VR
d
peak firing rate (Hz)
n.s.
e
stability
f
field size (cm)
g
Grid cells on a real linear track
mLT1-110811l-T2C1
L: stability = 0.711
R: stability = 0.084
mLT2-111101l-T1C1
L: stability = 0.286
R: stability = -0.001
mLT2-111025l-T1C2
L: stability = 0.004
R: stability = 0.368
mLT2-111024l-T1C1
L: stability = 0.731
R: stability = 0.466
mLT2-111025l-T1C1
L: stability = 0.595
R: stability = 0.338
mLT1-110810l-T1C2
L: stability = 0.565
R: stability = 0.688
mLT3-110929L-T1C1
L: stability = 0.278
R: stability = 0.372
mLT3-110930L-T2C1
L: stability = 0.400
R: stability = 0.568
mLT3-111020l-T1C1
L: stability = 0.714
R: stability = 0.969
mLT1-110810l-T1C1
L: stability = 0.497
R: stability = 0.622
sec
cm
h
grid cells
n.s.
stability
LT (n=64)
VR (n=96)

Supplementary Fig. 4: Comparisons of grid and border cells in open field (OF) and VR. **a-b)** Examples of grid (a) and border (b) cells recorded in OF and VR. The rate map for each cell in OF is shown on top. Bottom plot shows the same cell in VR, with average firing rate map shown on top and spike rasters over trials shown on bottom. Cells are labeled with cell ID (mxcy refers to mouse x, cell y) **c)** Mean firing rate during periods of movement (speed > 2 cm/s) increased in VR relative to OF for all cells, grid cells, and border cells (median (Hz) ± SEM, all cells: OF = 1.82 ± 0.22, VR = 2.15 ± 0.25, n = 781, Wilcoxon p = 1.6e-5; grid cells: OF = 1.45 ± 0.19, VR = 1.63 ± 0.36, n = 96, Wilcoxon p = 0.0028; border cells: OF = 1.36 ± 0.18, VR = 1.89 ± 0.38, n = 97, Wilcoxon p = 0.00016). In box plots, central line is the median, box edges are 25^{th} and 75^{th} percentiles, whiskers extend to the extremes of the distribution not considered to be outliers, and crosses display outliers. **d)** Peak firing rates increased in VR for all cells and border cells, but not grid cells (median (Hz) ± SEM, all cells: OF = 8.25 ± 0.35, VR = 9.16 ± 0.41, n = 781, Wilcoxon p = 1.6e-9; grid cells: OF = 8.40 ± 0.66, VR = 8.09 ± 0.75, n = 96, Wilcoxon p = 0.15; border cells: OF = 6.36 ± 0.60, VR = 8.06 ± 0.87, n = 97, Wilcoxon p = 0.0016). **e)** Stability increased in VR for all cells, but did not change in grid or border cells (median ± SD, all cells: OF = 0.40 ± 0.22, VR = 0.49 ± 0.25, n = 781, Wilcoxon p = 1.7e-11; grid cells: OF = 0.43 ± 0.25, VR = 0.41 ± 0.24, n = 96, Wilcoxon p = 0.14; border cells: OF = 0.50 ± 0.25, VR = 0.58 ± 0.24, n = 97, Wilcoxon p = 0.36). **f)** Grid cell field size significantly increased in VR (median ± SEM: OF = 12.2 ± 0.3 cm, VR = 18.0 ± 0.6 cm, n = 96, Wilcoxon p = 2.8e-12). **g)** Example grid cells recorded on a real linear track (LT). Data was taken from Eggink et al, 2014[22]. Red dots depict spikes and gray lines show the animal's trajectory. Each cell is labeled with its cell ID. **h)** Grid cell stability on the real linear track did not differ significantly from grid stability on our 1D VR track (median ± SD: LT = 0.39 ± 0.24, n = 64 grid cells, VR = 0.41 ± 0.24, n = 96 grid cells, Wilcoxon rank-sum test p = 0.91). n.s. not significant, ** $p < 0.01$, *** $p < 0.001$.

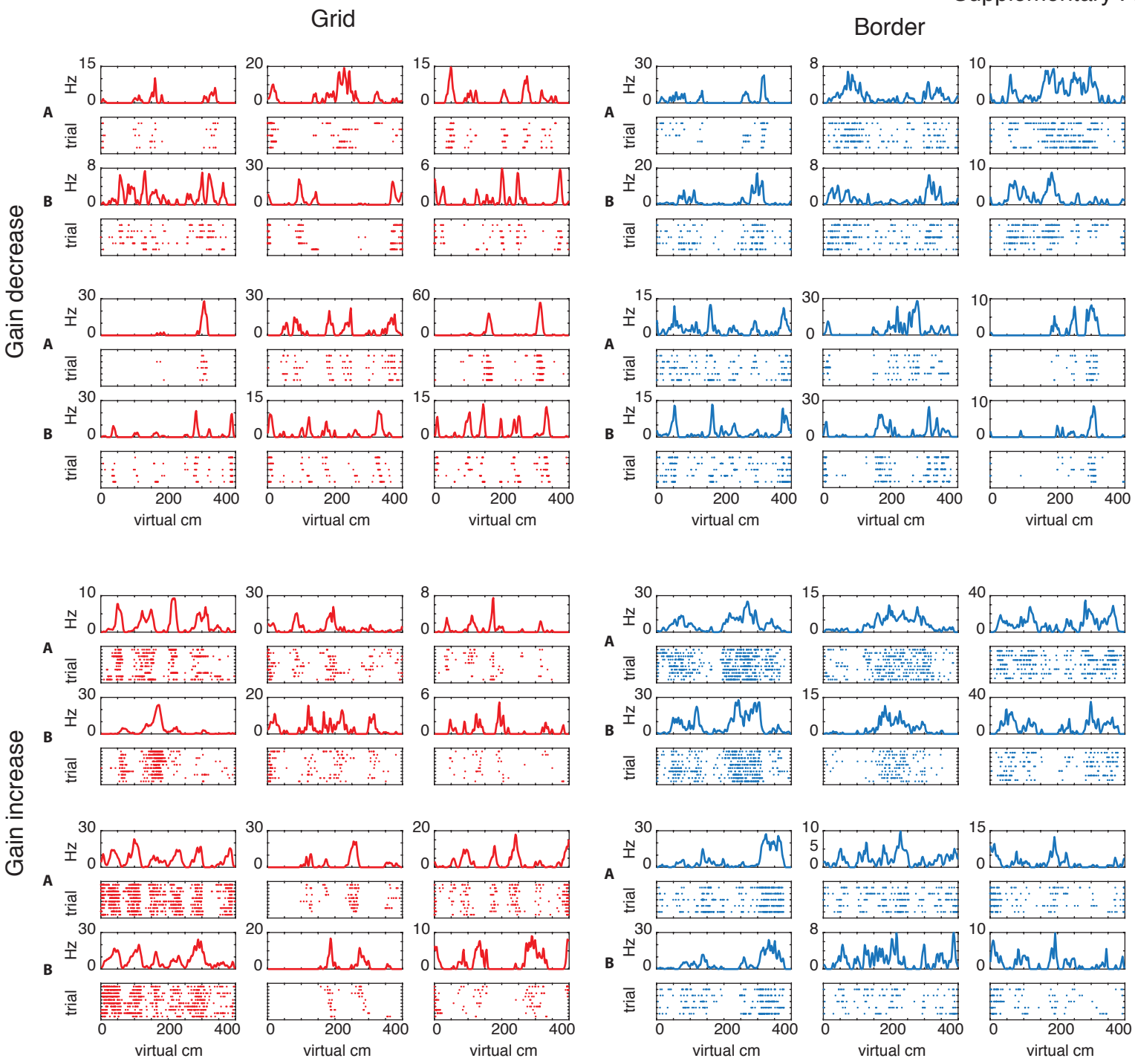

Supplementary Fig. 5: Additional examples of grid and border cells during VR gain changes (Fig. 2, 3). Data show firing rate (top panels) and spikes over trials (raster plots, bottom panels). The A period and B period have the same number of trials, with the A period defined as the *n* baseline trials preceding the B period, where *n* is the number of trials in the B period. Note that grid cells occasionally lost fields during gain increase, and that grid maps during gain decrease are not always scaled versions of baseline maps (see Supplementary Fig. 6e, g).

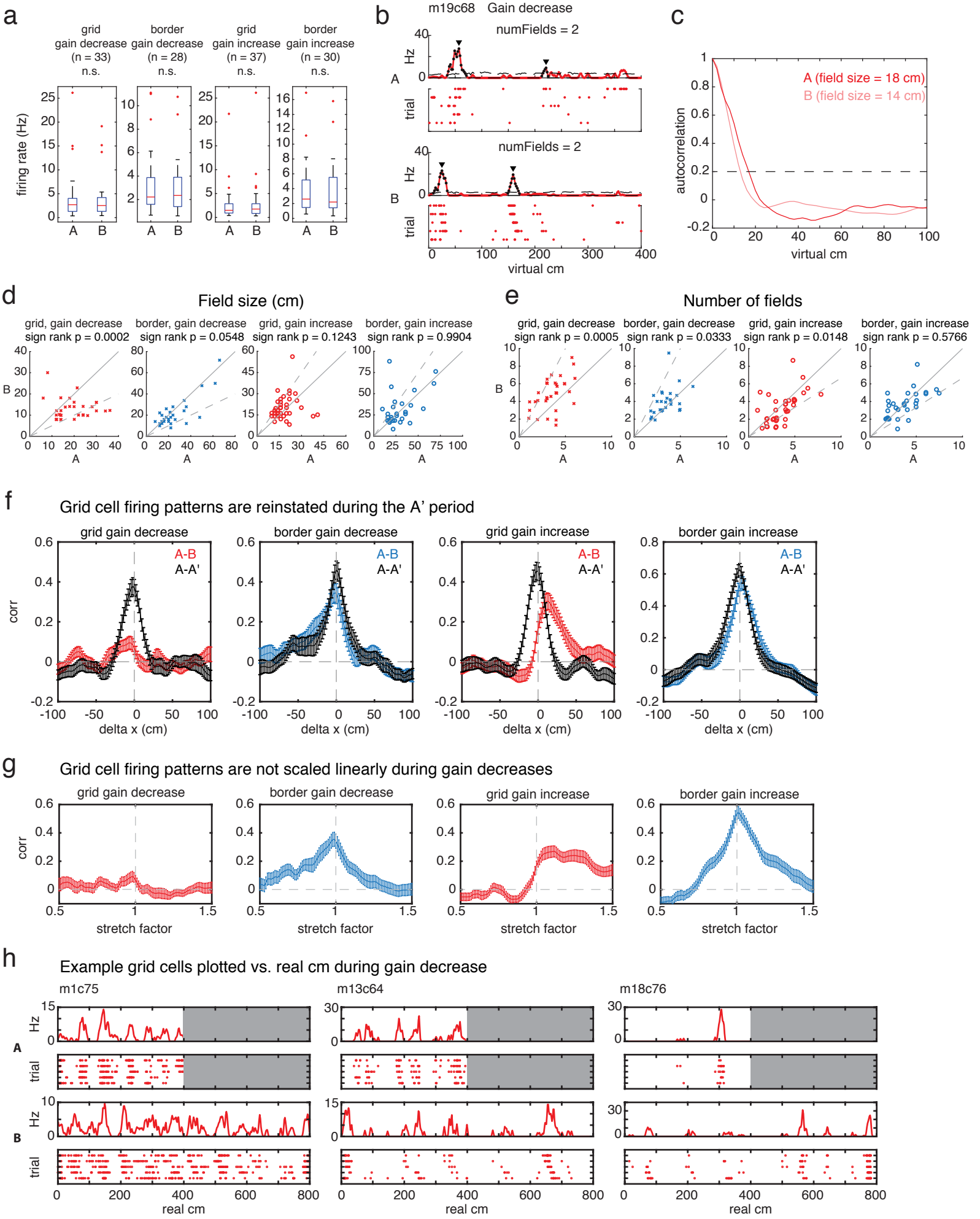
a
grid gain decrease (n = 33) n.s.
border gain decrease (n = 28) n.s.
grid gain increase (n = 37) n.s.
border gain increase (n = 30) n.s.
firing rate (Hz)
A
B
b
m19c68 Gain decrease
numFields = 2
numFields = 2
Hz
trial
virtual cm
c
A (field size = 18 cm)
B (field size = 14 cm)
autocorrelation
virtual cm
d
Field size (cm)
grid, gain decrease sign rank p = 0.0002
border, gain decrease sign rank p = 0.0548
grid, gain increase sign rank p = 0.1243
border, gain increase sign rank p = 0.9904
e
Number of fields
grid, gain decrease sign rank p = 0.0005
border, gain decrease sign rank p = 0.0333
grid, gain increase sign rank p = 0.0148
border, gain increase sign rank p = 0.5766
f
Grid cell firing patterns are reinstated during the A' period
grid gain decrease
border gain decrease
grid gain increase
border gain increase
A-B
A-A'
corr
delta x (cm)
g
Grid cell firing patterns are not scaled linearly during gain decreases
grid gain decrease
border gain decrease
grid gain increase
border gain increase
corr
stretch factor
h
Example grid cells plotted vs. real cm during gain decrease
m1c75
m13c64
m18c76
A
B
Hz
trial
real cm

Supplementary Fig. 6: Additional analyses of structural changes of grid and border cell rate maps during gain changes. **a)** Average firing rates during movement (speed > 2 cm/s) did not change during gain decreases or increases for either grid or border cells (median (Hz) ± SEM: grid gain decrease, A = 2.70 ± 0.90, B = 2.54 ± 0.73, n = 33, Wilcoxon p = 0.95; border gain decrease, A = 2.22 ± 0.54, B = 2.35 ± 0.46, n = 28, Wilcoxon p = 0.49; grid gain increase, A = 1.50 ± 0.60, B = 1.76 ± 0.72, n = 37, Wilcoxon p = 0.36; border gain increase, A = 2.60 ± 0.65, B = 2.20 ± 0.65, n = 30, Wilcoxon p = 0.70). In box plots, central line is the median, box edges are 25^{th} and 75^{th} percentiles, whiskers extend to the extremes of the distribution not considered to be outliers, and dots display outliers. **b)** An example grid cell during gain decrease with field detection shown. Briefly, spikes were shuffled within-trial to create percentiles of a shuffled firing rate distribution that was used to define fields (Online Methods), which we then counted (numFields). The cell is labeled with cell ID (mxcy refers to mouse x, cell y). **c)** Autocorrelation of the firing rate in the A and B period of the cell shown in (b). Field size was defined as the point at which the autocorrelation fell below 0.2. **d)** Consistent with the population measure (Fig. 3c), field size decreased for grid cells during gain decrease but did not change for grid cells in gain increase or border cells in either gain change (mean (cm) ± SEM: grid gain decrease, A = 19.0 ± 1.3, B = 12.8 ± 0.8, n = 33, Wilcoxon p = 0.00023; border gain decrease, A = 25.8 ± 2.8, B = 22.1 ± 2.7, n = 28, Wilcoxon p = 0.055; grid gain increase, A = 18.6 ± 1.1, B = 20.3 ± 1.4, n = 37, Wilcoxon p = 0.12; border gain increase, A = 28.7 ± 2.8, B = 30.8 ± 3.5, n = 30, Wilcoxon p = 0.99; means presented instead of medians because values were discretized). Scatterplots show field size for individual grid (red) and border (blue) cells in baseline (A) and gain manipulation (B) sessions. The dashed line is the predicted response if the spatial firing pattern was only driven by locomotor cues and the solid line is the predicted response if the spatial firing pattern was only driven by visual cues. **e)** Number of significant firing fields during baseline and gain change. Here, grid cell field numbers increased in gain decrease, and decreased in gain increase. Occasionally, phase shifts in grid cells would be accompanied by a loss of one or more fields (see examples in Supplementary Fig. 5), explaining the existence of both phase shifts and loss of fields. Border cells also increased in number of fields during gain decreases (mean ± SEM: grid gain decrease, A = 3.58 ± 0.25, B = 4.86 ± 0.32, n = 33, Wilcoxon p = 0.00046; border gain decrease, A = 3.43 ± 0.22, B = 3.97 ± 0.28, n = 28, Wilcoxon p = 0.033; grid gain increase, A = 3.59 ± 0.25, B = 3.15 ± 0.28, n = 37, Wilcoxon p = 0.015; border gain increase, A = 3.75 ± 0.30, B = 3.65 ± 0.27, n = 30, Wilcoxon p = 0.58). Scatterplots shown as in (d). **f)** Comparison of A-B cross-correlation with A-A' cross-correlation, where A' is the matched number of trials immediately following B. A period grid patterns were re-instated following gain

changes, as can be seen from the large peaks at 0 lag in the cross-correlation between A and A'. Error bars: mean ± SEM. **g)** Correlations between A and B period rate maps when the A period rate map was scaled by different amounts, from 0.5 to 1.5. If the grid map in B was a simple rescaling of the map in A, one would expect a large peak at a stretch factor between 0.5 and 1 (far left panel). The lack of such a peak shows that grid remapping during gain decreases was not a simple rescaling of the A period pattern, but rather reflected the formation of a new map with smaller scale. The large hump to the right of zero in grid gain increases (middle, right) is expected from the phase shifts seen in this condition (Fig. 3b). Error bars: mean ± SEM. **h)** Example grid cells during gain decreases plotted versus real cm as opposed to virtual cm. Note that the firing rate maps do not perfectly align, and that occasionally new fields appear or fields are lost. This shows that gain decrease responses were not a linear re-scaling of baseline patterns. Error bars: mean ± SEM.

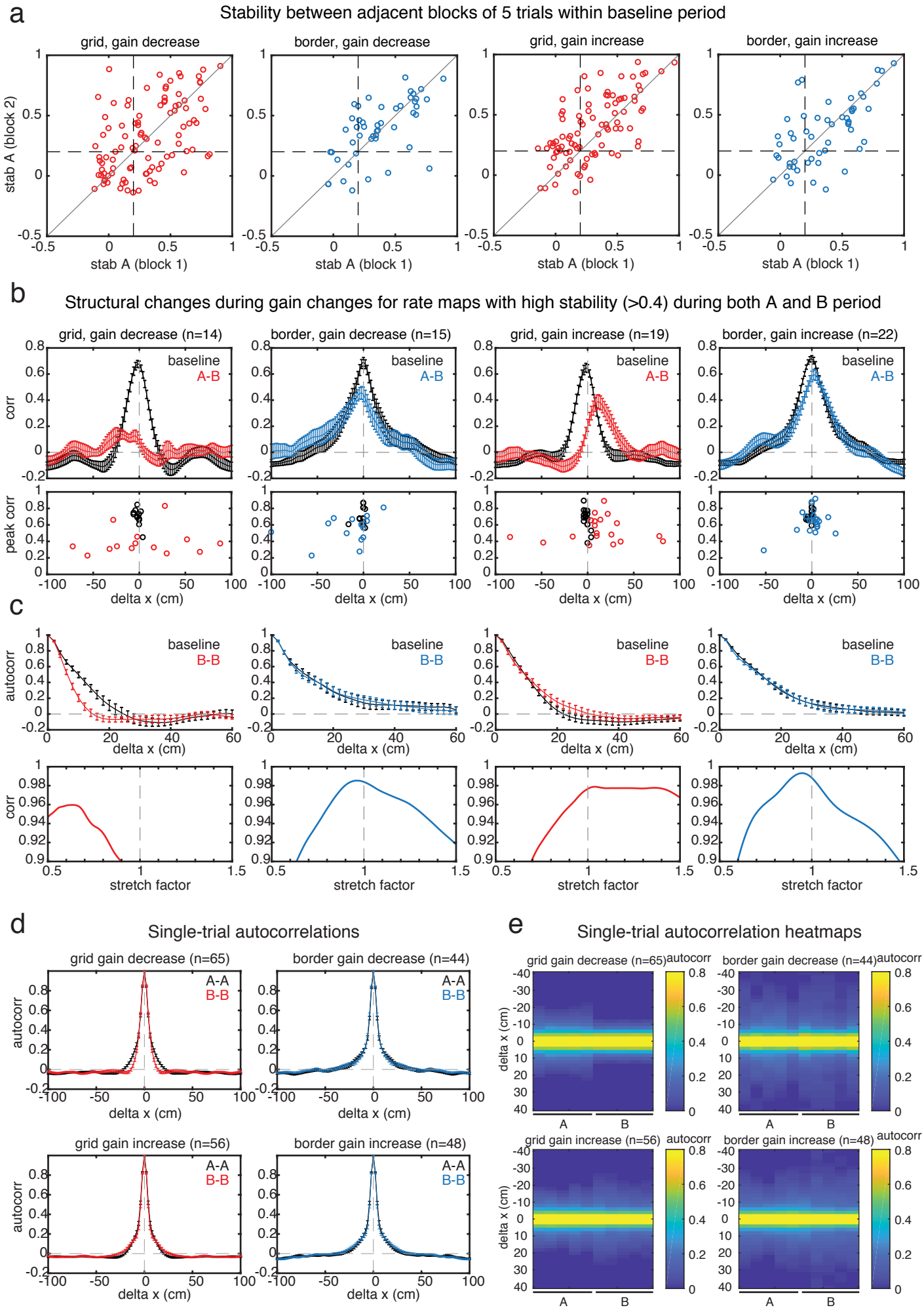
a
Stability between adjacent blocks of 5 trials within baseline period
grid, gain decrease
border, gain decrease
grid, gain increase
border, gain increase
stab A (block 2)
stab A (block 1)
b
Structural changes during gain changes for rate maps with high stability (>0.4) during both A and B period
grid, gain decrease (n=14)
border, gain decrease (n=15)
grid, gain increase (n=19)
border, gain increase (n=22)
baseline
A-B
corr
peak corr
delta x (cm)
c
baseline
B-B
autocorr
delta x (cm)
corr
stretch factor
d
Single-trial autocorrelations
grid gain decrease (n=65)
border gain decrease (n=44)
grid gain increase (n=56)
border gain increase (n=48)
A-A
B-B
autocorr
delta x (cm)
e
Single-trial autocorrelation heatmaps
grid gain decrease (n=65)
border gain decrease (n=44)
grid gain increase (n=56)
border gain increase (n=48)
autocorr
delta x (cm)
A
B

Supplementary Fig. 7: Structural changes during gain manipulations are not driven by instability of the grid patterns in the B period. **a)** Stability computed in the block of 5 trials immediately preceding the B period of gain manipulations (block 2) and the 5 trials preceding those (block 1) (mean ± SD: grid gain decrease, block 1 = 0.31 ± 0.30, block 2 = 0.32 ± 0.30, n = 98 pairs of blocks from 67 cells, Wilcoxon p = 0.80; border gain decrease, block 1 = 0.37 ± 0.28, block 2 = 0.39 ± 0.28, n = 48 pairs of blocks from 44 cells, Wilcoxon p = 0.31; grid gain increase, block 1 = 0.30 ± 0.29, block 2 = 0.39 ± 0.29, n = 91 pairs of blocks from 55 cells, Wilcoxon p = 0.0007; border gain increase, block 1 = 0.36 ± 0.29, block 2 = 0.35 ± 0.29, n = 52 pairs of blocks from 47 cells, Wilcoxon p = 0.60). The percentage of cells with at least one pair of stable baseline blocks was similar to the percentage of cells with at least one stable gain manipulation (grid gain decrease, baseline: 36/67 (54%), gain change: 33/65 (51%); grid gain increase, baseline: 31/55 (56%), gain change: 37/56 (66%); border gain decrease, baseline: 29/44 (66%), gain change: 28/44 (64%); border gain increase, baseline: 27/47 (57%), gain change: 30/48 (63%)). Therefore, degeneration during gain changes was comparable to baseline instability. Note that the number of gain manipulations and cells differs slightly between baseline and gain change because we applied the same firing rate threshold of 0.2 Hz to both periods, resulting in the inclusion of a small number of manipulations that had firing rate < 0.2 Hz in B but firing rate > 0.2 Hz in block 1, and vice versa. **b)** and **c)** Structural changes in grid and border cells that were highly stable (stability > 0.4) in both the A period and B period of gain manipulations. Results were qualitatively identical to those in Figure 3, indicating that instability was not driving the structural changes we observed during gain changes. Error bars: mean ± SEM. **d)** Population average of single-trial autocorrelation of firing rate for grid and border cells in gain decrease and increase (Online Methods). This method allowed the inclusion of unstable cells, since it did not compare spiking patterns across trials. The reduction in autocorrelation width during gain decrease, with no change in any other condition, is consistent with the full period analysis (Fig. 3). Error bars: mean ± SEM. **e)** Heatmaps showing average single-trial autocorrelations for each individual trial in the 5 trials preceding and 5 trials following the gain change. Note the abrupt change to a new scale following the gain decrease for grid cells and the relative lack of change for grid or border cells in the other conditions.

a

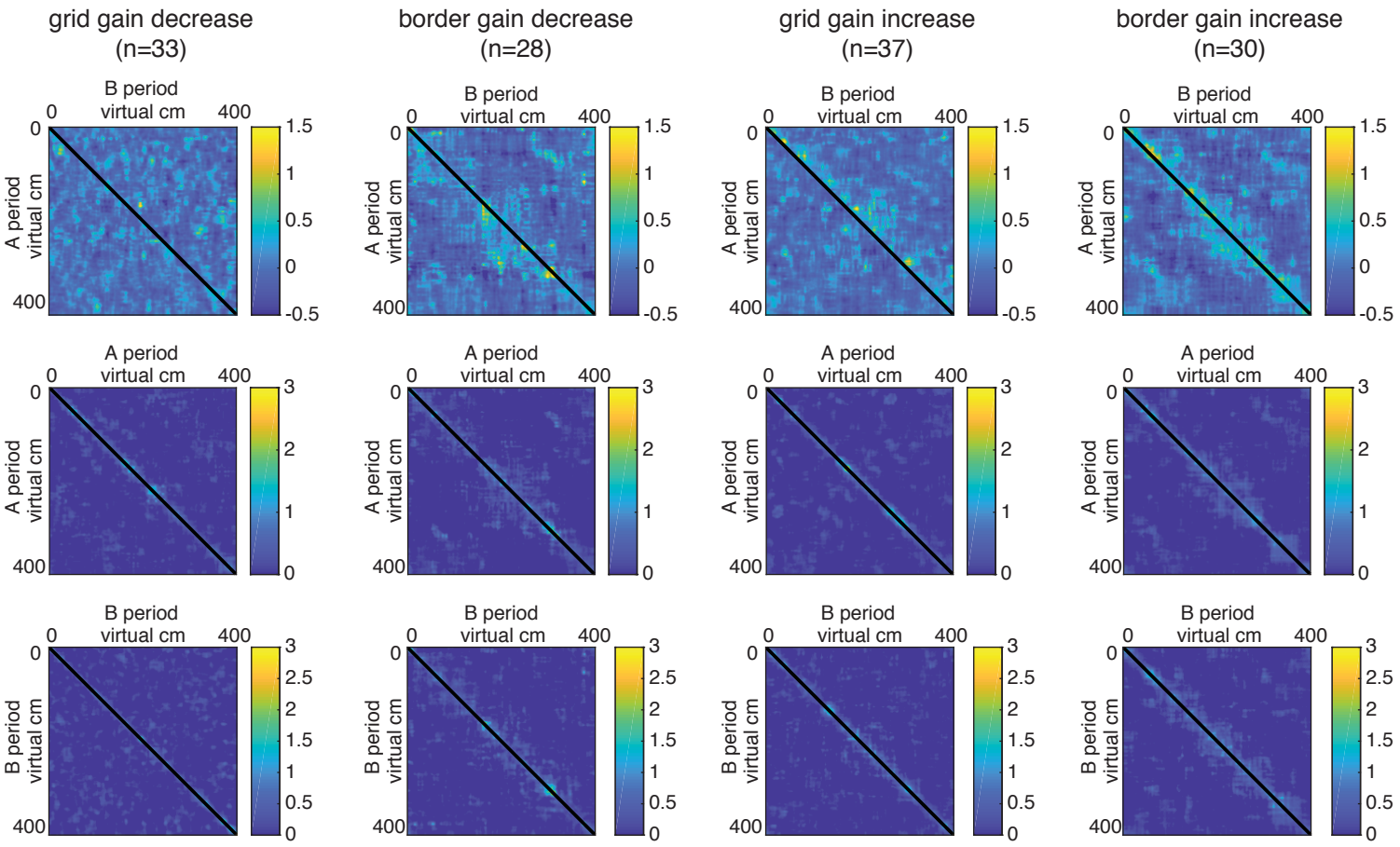
grid gain decrease (n=33)
border gain decrease (n=28)
grid gain increase (n=37)
border gain increase (n=30)
B period virtual cm
A period virtual cm
A period virtual cm
B period virtual cm
0
400
1.5
1
0.5
0
-0.5
3
2
1
0
2.5
1.5
0.5

b

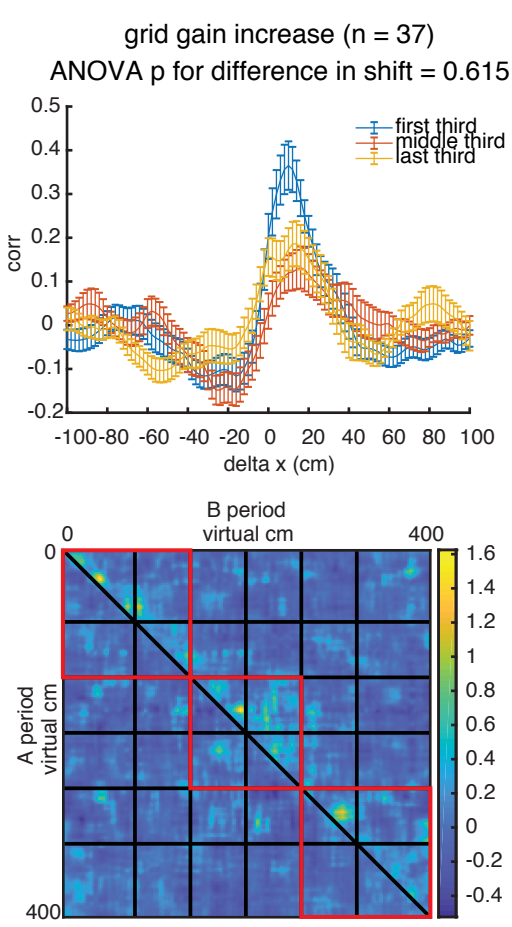
grid gain increase (n = 37)
ANOVA p for difference in shift = 0.615
first third
middle third
last third
corr
delta x (cm)
B period virtual cm
A period virtual cm
0
400
1.6
1.4
1.2
1
0.8
0.6
0.4
0.2
0
-0.2
-0.4

c

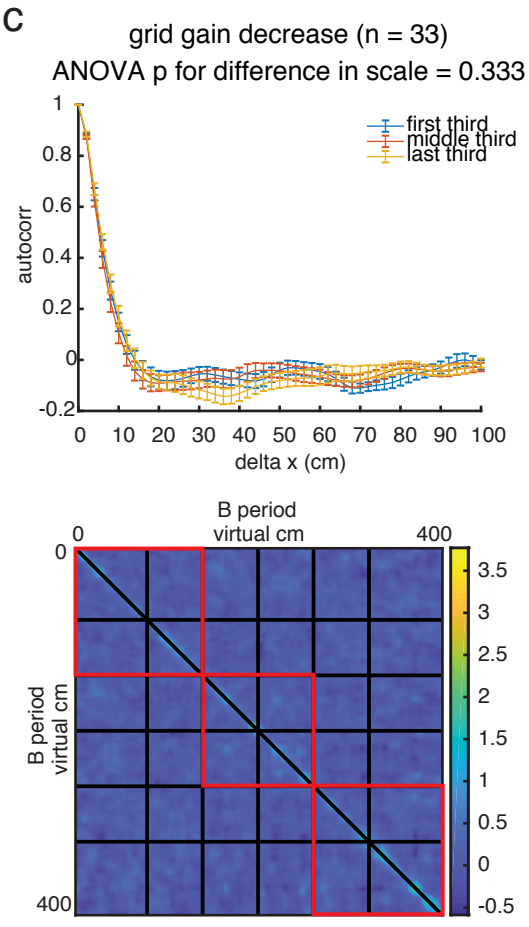
grid gain decrease (n = 33)
ANOVA p for difference in scale = 0.333
first third
middle third
last third
autocorr
delta x (cm)
B period virtual cm
B period virtual cm
0
400
3.5
3
2.5
2
1.5
1
0.5
0
-0.5

Supplementary Fig. 8: Grid cell structural changes during gain changes were uniform over the track, suggesting that the strength of landmark input was approximately constant along the track. This rules out the possibility that non-uniformity in landmark input could cause larger decoherence during the gain decrease condition than the gain increase condition. **a)** Average outer products between firing rate vectors in baseline (A) and gain change (B) for grid and border cells. The color of pixel (*i*,*j*) in the matrix is a unitless quantity that is the average product of the normalized firing rate at positions x_i and x_j (Online Methods). Cross-correlations and auto-correlations are normalized projections of these matrices along the diagonal (Fig. 3); these maps give a complete picture of the structural changes across different locations on the track. Note the density above the diagonal in the A-B outer product for grid gain increase. This corresponds to the phase shift in grid firing patterns during gain increase (Fig. 3b). Note also the slightly narrower band around the diagonal for grid gain decrease in the B-B outer product compared to the A-A outer product. This corresponds to the rescaling of grid cells during gain decrease (Fig. 3c). **b)** Top: Grid cell gain increase A-B correlation in the first, middle, and last segments of the track, corresponding to regions with different patterns on the walls (see Fig. 1). The amount of rightward shift in cm did not differ between the three segments of the track (gain increase, A-B cross-correlation shift: first third = 9.1 ± 4.9 cm, middle third = 3.1 ± 9.0 cm, last third = 13.7 ± 8.1 cm, n = 37 cells, ANOVA for difference in shift $p = 0.62$). Error bars: mean ± SEM. Bottom: average outer product between the A and B period firing rate vectors. The three regions analyzed (first, middle, last) are highlighted in red. Vertical and horizontal black lines indicate locations of the landmarks. **c)** Top: The amount of rescaling in grid cells in gain decrease sessions did not differ between the three segments of the track (gain decrease, B-B autocorrelation width: first third = 11.9 ± 0.9 cm, middle third = 10.3 ± 0.7 cm, last third = 11.5 ± 0.7 cm, n = 33 cells, ANOVA for difference in scale $p = 0.33$). Error bars: mean ± SEM. Bottom: the outer product matrix between the grid gain decrease B period firing rate and itself.

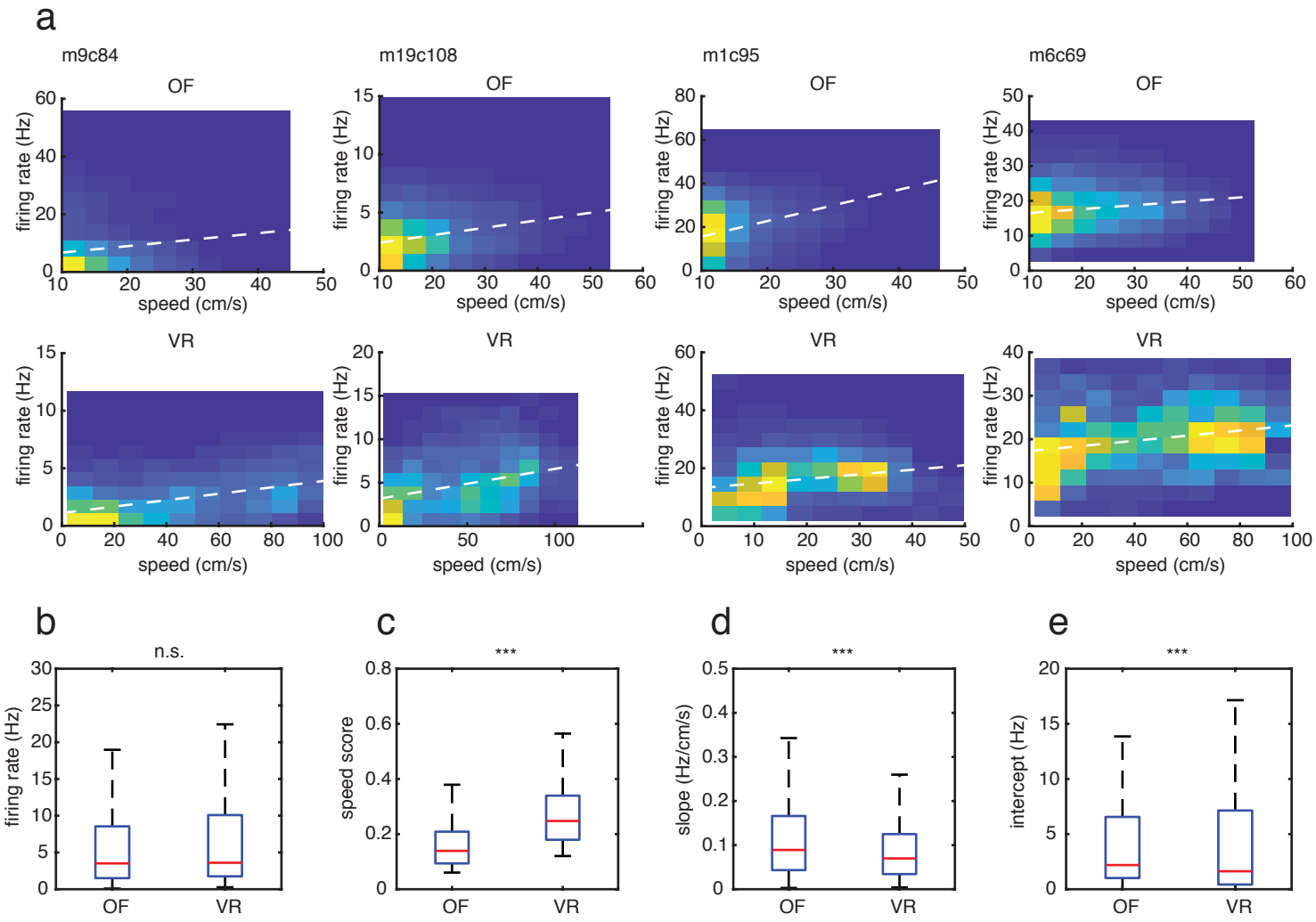

Supplementary Fig. 9: Comparisons of speed cells between open field (OF) and VR. To be included here, cells had to pass speed criteria in both OF and VR (Online Methods). Note that running speeds were higher in VR compared to OF (Supplementary Fig. 2). **a)** Example speed cells in OF and VR. Heat map colors are proportional to the amount of time the running speed and firing speed were in the corresponding bin. White dotted lines show linear regression fits to data. **b)** Speed cell firing rates did not change between OF and VR (median (Hz) ± SEM: OF = 3.52 ± 0.60, VR = 3.60 ± 0.61, n = 171, Wilcoxon p = 0.15). In box plots, the red line is the median, edges of the box are the 25th and 75th percentiles, and the whiskers extend to the extremes of the distribution not considered to be outliers by the algorithm. Outliers are omitted for clarity. **c)** Speed scores increased in VR (median ± SEM: OF = 0.139 ± 0.008, VR = 0.248 ± 0.010, n = 171, Wilcoxon p = 5.2e-19). **d)** Speed cell slopes decreased in VR (median (Hz/cm/s) ± SEM: OF = 0.0891 ± 0.0151, VR = 0.0699 ± 0.0075, n = 171, Wilcoxon p = 5.5e-5), consistent with the expansion of grid cells in VR (Supplementary Fig. 4f). **e)** Speed cell intercepts decreased in VR (median (Hz) ± SEM: OF = 2.19 ± 0.52, VR = 1.63 ± 0.52, n = 171, Wilcoxon p = 0.00099). *** $p < 0.001$.

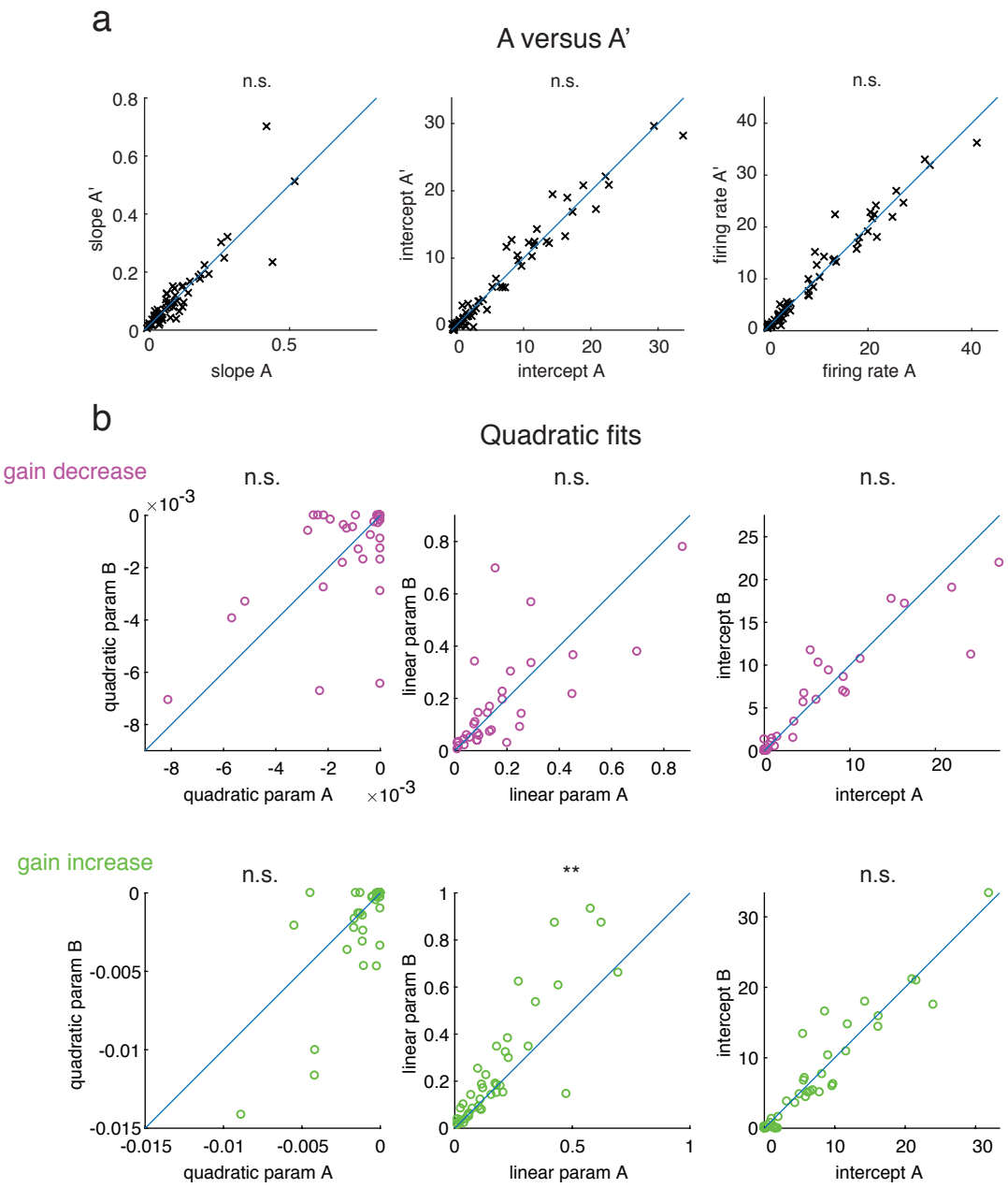

Supplementary Fig. 10: Additional speed cell gain change analyses. **a)** Analysis of speed cell changes from the A period to the first 10 trials of the A' period. Cells had to pass speed cell criteria in both the A period and the first 10 trials of the A' period. Left: slopes of linear fits did not change (median (Hz/cm/s) ± SEM: A = 0.076 ± 0.013, A' = 0.076 ± 0.015, n = 61, Wilcoxon p = 0.88). Middle: intercepts of linear fits did not change (median (Hz) ± SEM: A = 3.3 ± 1.0, A' = 3.2 ± 1.0, n = 61, Wilcoxon p = 0.79). Right: firing rates did not change (median (Hz) ± SEM: A = 5.0 ± 1.2, A' = 5.3 ± 1.2, n = 61, Wilcoxon p = 0.88). These results rule out effects from differing numbers of trials or slow changes over time. **b)** Quadratic fits to data to account for saturation of firing rate. The quadratic constant was constrained to be negative and linear and intercept parameters were constrained to be non-negative (enforcing a saturating shape). As observed with linear fits (Fig. 4), the only significant change was in the linear parameter during gain increases (g.i. linear parameter p = 0.0057; g.i. intercept p = 0.16; g.i. quadratic parameter p = 0.13; g.d. linear parameter p = 0.60; g.d. intercept p = 0.83; g.d. quadratic parameter p = 0.72; n = 33 gain decrease (g.d.), 41 gain increase (g.i.); Wilcoxon tests). n.s. not significant, ** p < 0.01, *** p < 0.001.

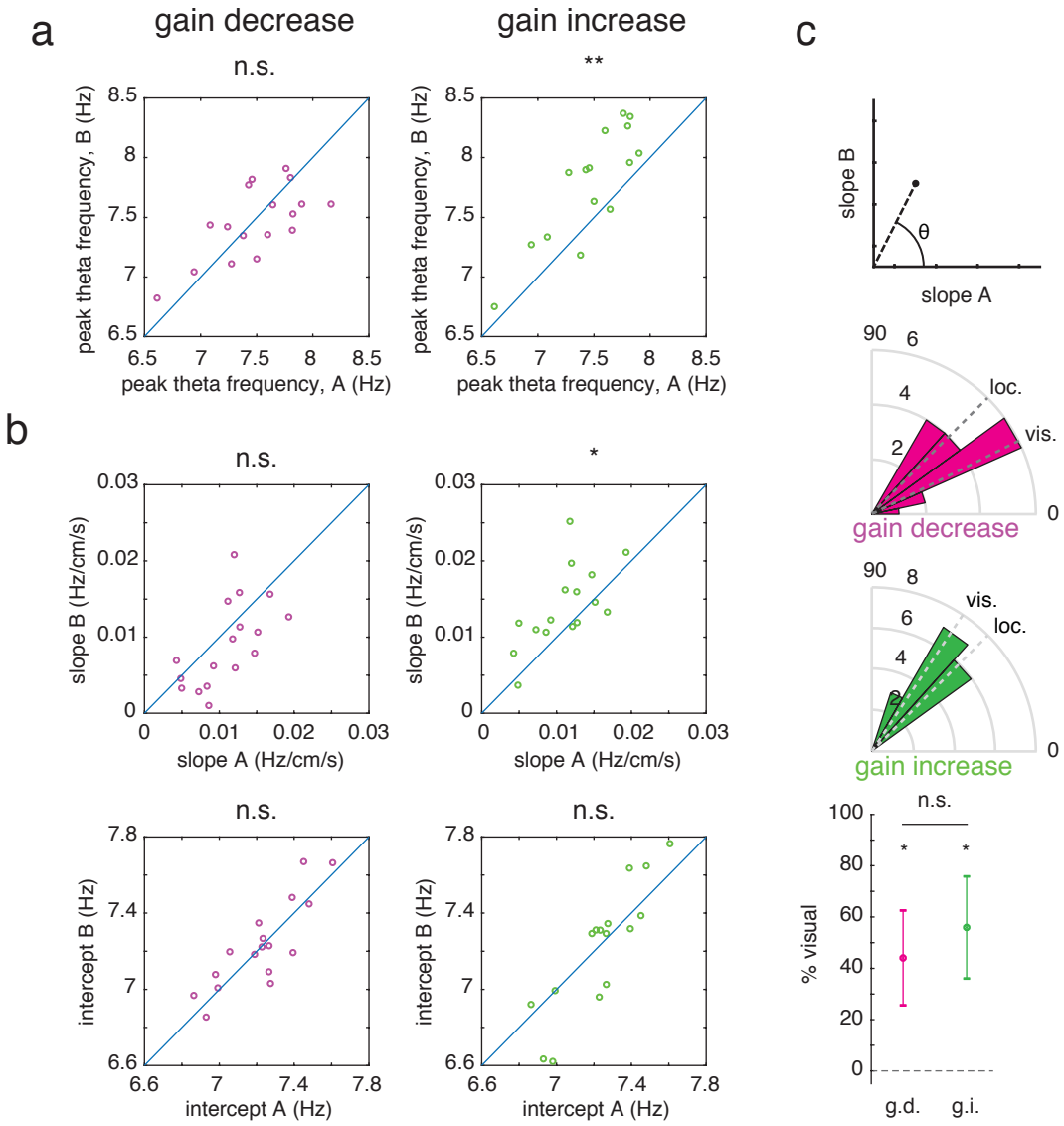
a
gain decrease
gain increase
n.s.
**
peak theta frequency, B (Hz)
peak theta frequency, A (Hz)
b
n.s.
*
slope B (Hz/cm/s)
slope A (Hz/cm/s)
n.s.
n.s.
intercept B (Hz)
intercept A (Hz)
c
slope B
θ
slope A
loc.
vis.
gain decrease
gain increase
n.s.
% visual
g.d.
g.i.

Supplementary Fig. 11: LFP theta response to gain manipulations. Sessions with significant theta power were concatenated by mouse (158/187 gain manipulation sessions; Online Methods). **a)** Theta frequency of peak power increased during gain increases but did not change during gain decreases (peak frequency (Hz) ± SEM: gain increase A = 7.51 ± 0.10, B = 7.82 ± 0.13, n = 16 mice, Wilcoxon p = 0.0016; gain decrease A = 7.50 ± 0.09 Hz, B = 7.45 ± 0.07, n = 17 mice, Wilcoxon p = 0.59). **b)** Parameters of linear fits between instantaneous theta frequency and running speed. Slopes of linear fits increased during gain increases but did not change during gain decreases (slope (Hz/cm/s) ± SEM: gain decrease, A = 0.0110 ± 0.0010, B = 0.0090 ± 0.0013, n = 17 mice, Wilcoxon p = 0.076; gain increase, A = 0.0111 ± 0.0011, B = 0.0140 ± 0.0013, n = 16 mice, Wilcoxon p = 0.015). Intercepts did not change in either case (intercept (Hz) ± SEM: gain decrease, A = 7.23 ± 0.05, B = 7.23 ± 0.06, n = 17 mice, Wilcoxon p = 0.69; gain increase, A = 7.24 ± 0.05, B = 7.21 ± 0.06, n = 16 mice, Wilcoxon p = 0.88). **c)** Slope changes were converted into angles (as in Fig. 4), with full locomotor weighting corresponding to an angle of 45^0, and full visual weighting corresponding to arctan (0.5), or 26.6^0, in gain decrease, and arctan (1.5), or 56.3°, in gain increase. Top panel: Illustration of conversion of slope changes into an angle between 0 and 90°. Middle two panels: Average angles were 36.9 ± 3.4^0 for gain decrease (pink) and 51.3 ± 2.3^0 for gain increase (green) (mean ± SEM). Bottom panel: Expressed as percentages, this corresponds to 44 ± 18% visual weighting in gain decrease and 56 ± 20% visual weighting in gain increase (mean ± SEM). These percentages were significantly greater than zero (gain decrease Wilcoxon p = 0.044; gain increase Wilcoxon p = 0.023), but did not differ (p = 0.64, Wilcoxon test on 16 mice with both gain decrease and gain increase sessions). Therefore, though effects on peak frequency were more pronounced in gain increases versus gain decreases, visual weights of theta frequency were not significantly higher for gain increases than gain decreases. gd = gain decrease, gi = gain increase, n.s. = not significant, * $p < 0.05$, ** $p < 0.01$.

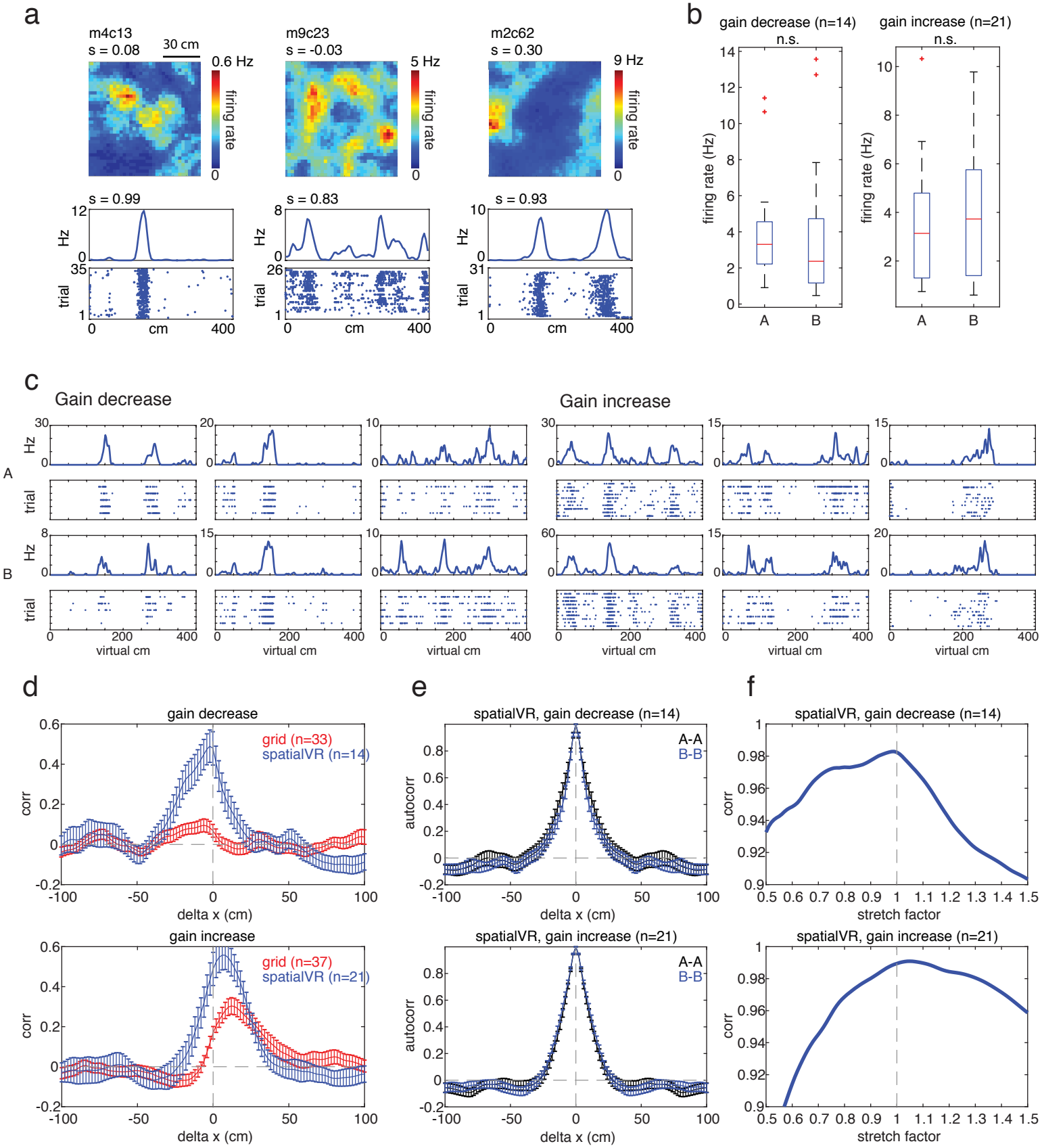
a
m4c13
s = 0.08
30 cm
0.6 Hz
firing rate
0
m9c23
s = -0.03
5 Hz
m2c62
s = 0.30
9 Hz
s = 0.99
s = 0.83
s = 0.93
Hz
trial
cm
b
gain decrease (n=14)
n.s.
gain increase (n=21)
firing rate (Hz)
A
B
c
Gain decrease
Gain increase
virtual cm
d
gain decrease
grid (n=33)
spatialVR (n=14)
corr
delta x (cm)
gain increase
grid (n=37)
spatialVR (n=21)
e
spatialVR, gain decrease (n=14)
A-A
B-B
autocorr
spatialVR, gain increase (n=21)
f
stretch factor

Supplementary Fig. 12: Spatially stable VR cells during gain manipulations. Spatially stable VR cells were defined as cells that were not grid, border, or head direction cells in the open field (OF) but had spatial stability > 0.5 in both the A period and B period. **a)** Examples of spatially stable VR cells in OF and VR. Top: firing rate map in OF. Cells are labeled with cell ID (mxcy refers to mouse x, cell y). Bottom: firing map on the VR linear track with firing rate shown in the top panel and spikes over trials (raster plots) shown in the bottom panel. s = stability. Many cells were highly stable in VR but not OF. **b)** Spatially stable VR cell firing rates did not change during either gain decreases or gain increases (median (Hz) ± SEM: gain decrease, A = 3.3 ± 0.9, B = 2.4 ± 1.1, n = 14, Wilcoxon p = 0.67; gain increase A = 3.1 ± 0.5, B = 3.7 ± 0.5, n = 21, Wilcoxon p = 0.69). In box plots, the red line is the median, edges of the box are the 25th and 75th percentiles, whiskers extend to the most extreme non-outlier data points, and outliers are plotted individually (red crosses). **c)** Examples of three spatially stable VR cells on gain decrease (left) and gain increase (right) manipulations. Each column shows data from the same neuron. Firing rate maps shown as in (a). **d-f)** Same as Figure 3b-c, but for spatially stable VR cells, with grid cells plotted for comparison. Like border cells, spatially stable VR cells were primarily driven by visual landmark cues in VR. n.s. = not significant. Error bars: mean ± SEM.

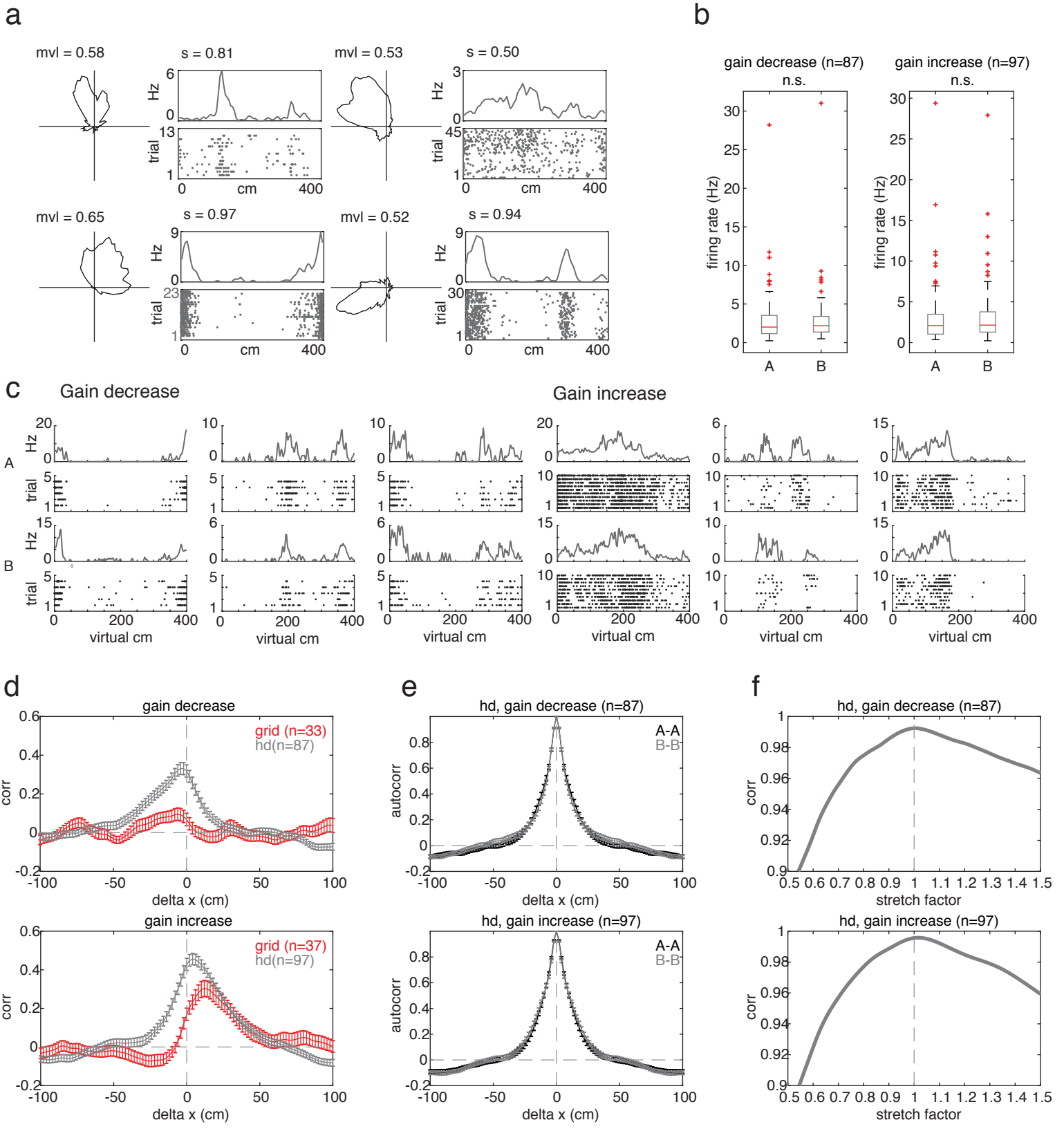
a
mvl = 0.58
s = 0.81
mvl = 0.53
s = 0.50
mvl = 0.65
s = 0.97
mvl = 0.52
s = 0.94
Hz
trial
cm
b
gain decrease (n=87)
gain increase (n=97)
n.s.
firing rate (Hz)
A
B
c
Gain decrease
Gain increase
A
B
virtual cm
d
gain decrease
grid (n=33)
hd(n=87)
gain increase
grid (n=37)
hd(n=97)
corr
delta x (cm)
e
hd, gain decrease (n=87)
hd, gain increase (n=97)
A-A
B-B
autocorr
f
stretch factor

Supplementary Fig. 13: Head direction cells during gain manipulations. Head direction cells were defined as having mean vector length > 0.154 and mean firing rate < 10 Hz in the open field (OF) **a)** Example head direction cells in OF and VR. Left: directional firing rate of a head direction cell expressed as a polar plot of head direction in the open field. Right: firing map on the VR linear track with firing rate shown in the top panel and spikes over trials (raster plots) shown in the bottom panel. mvl = mean vector length from OF recording, s = stability in VR recording. **b)** Head direction cell firing rates did not change during either gain decreases or gain increases (median (Hz) ± SEM: gain decrease, A = 2.0 ± 0.4, B = 2.2 ± 0.4, n = 87, Wilcoxon p = 0.29; gain increase A = 2.1 ± 0.4, B = 2.1 ± 0.4, n = 97, Wilcoxon p = 0.17). In box plots, the red line is the median, edges of the box are the 25th and 75th percentiles, whiskers extend to the most extreme non-outlier data points, and outliers are plotted individually. **c)** Example head direction cell response to gain decreases (left) and gain increases (right). Firing rate maps shown as in (a). **d-f)** Same as Figure 3b-c, but for head direction cells, with grid cells plotted for comparison. As for grid and border cells, only stable recordings were kept for this analysis (stability > 0.2 in both A and B period). Like border cells, head direction cells were primarily driven by visual landmark cues in VR. n.s. = not significant. Error bars: mean ± SEM.

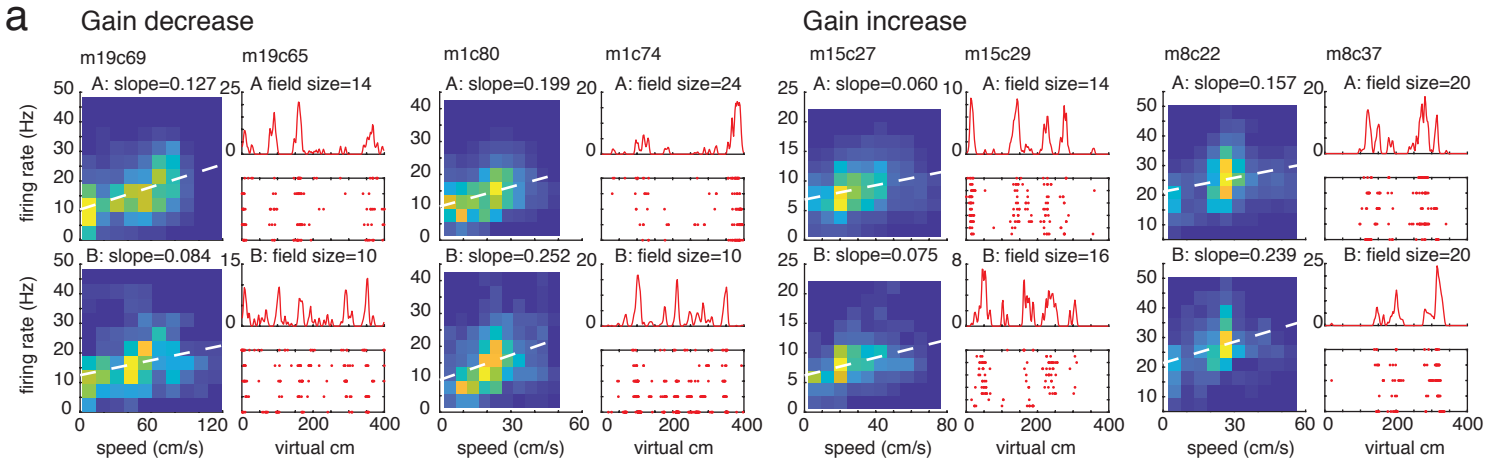
a
Gain decrease
Gain increase
m19c69
m19c65
m1c80
m1c74
m15c27
m15c29
m8c22
m8c37
A: slope=0.127
A field size=14
A: slope=0.199
A: field size=24
A: slope=0.060
A: field size=14
A: slope=0.157
A: field size=20
B: slope=0.084
B: field size=10
B: slope=0.252
B: field size=10
B: slope=0.075
B: field size=16
B: slope=0.239
B: field size=20
firing rate (Hz)
speed (cm/s)
virtual cm

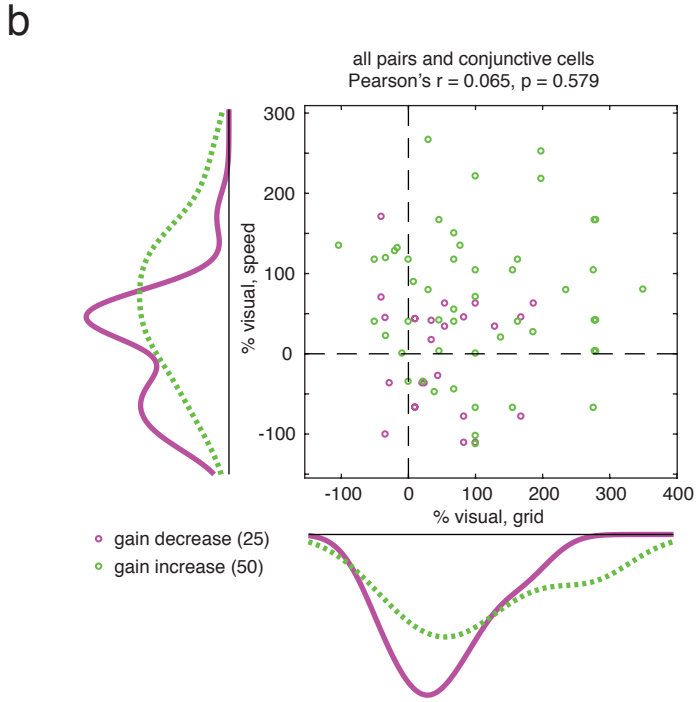
b
all pairs and conjunctive cells
Pearson's r = 0.065, p = 0.579
% visual, speed
% visual, grid
gain decrease (25)
gain increase (50)

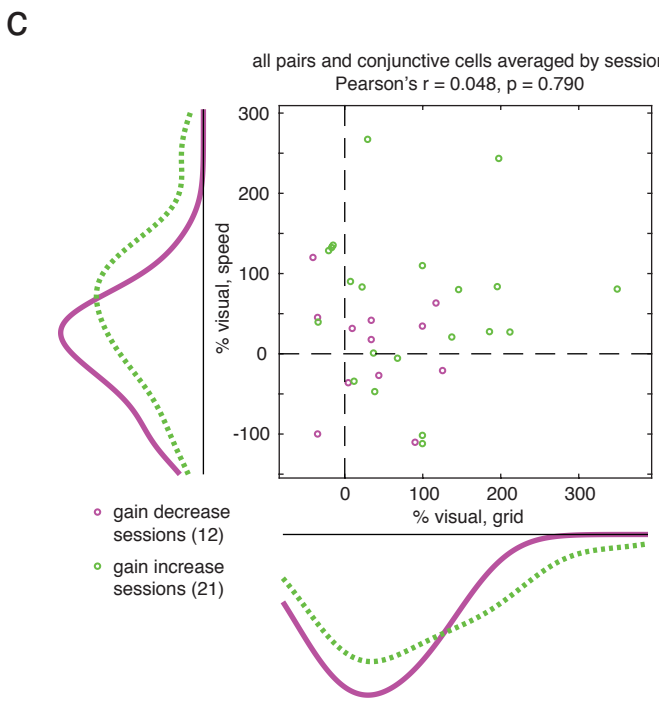
c
all pairs and conjunctive cells averaged by session
Pearson's r = 0.048, p = 0.790
% visual, speed
% visual, grid
gain decrease sessions (12)
gain increase sessions (21)

Supplementary Fig. 14: Pairs of simultaneously recorded speed and grid cells during gain manipulations. **a)** Example pairs for gain decrease (left) and gain increase (right). Grid cell data show firing rate (top panel) and spikes over trials (raster plots, bottom panel). Speed cell data are plotted as a heat map of instantaneous firing rate with respect to running speed, with colors indicating the percentage of time bins with the corresponding firing rate and running speed. Grid cell field sizes were calculated based on the autocorrelation function of the firing rate map (Online Methods). **b)** Percent visual weights for all pairs of simultaneously recorded speed and grid cells, estimated based on slope changes (as in Fig. 4) and field size changes (as in Supplementary Fig. 6c, d). Slope and field size changes were converted to angles, with an angle of 45^0 and full visual weighting corresponding and full visual weighting corresponding to arctan (0.5), or 26.6^0, in gain decrease, and arctan (1.5), or 56.3^0, in gain increase. Before computing angles, grid cell field sizes were converted into real cm (by dividing by the gain factor) to compare with speed cell slopes, which were computed relative to real running speed. The percent weighting of visual cues was uncorrelated between individual pairs of grid and speed cells (Pearson's r = 0.065, p = 0.58, n = 75 pairs, 25 gain decrease, 50 gain increase from 26 grid cells, 17 speed cells, and 11 conjunctive grid x speed cells; 58 unique pairs), but the average responses of grid and speed cells were consistent with the population, with gain increases having higher visual weights than gain decreases for both grid and speed cells (marginal histograms; pink = gain decrease, green = gain increase; Fig. 3 and 4). This shows that while, as populations, speed and grid cells behaved consistently, they were uncorrelated on a cell-by-cell basis. **c)** The same was true when speed and grid cells were averaged by session (Pearson's r = 0.048, p = 0.79, n = 33 sessions, 12 gain decrease, 21 gain increase). These results suggest that grid cells either i) integrate input from many speed cells, ii) integrate input from a specific subset of speed cells, or iii) receive input from another source. Notably, several recent works have demonstrated that speed cells show high degrees of heterogeneity, with their firing rates showing positive or negative linear, saturating and even non-monotonic relationships with running speed[7,8,23]. These levels of heterogeneity present a significant challenge for attractor-based grid cell network models, which often require inputs that are positively and linearly modulated by running speed. One way to overcome this challenge would be to assume grid cells integrate a population vector of speed inputs. This population vector could consist of signals from MEC speed cells as well as speed signals such as changes in theta frequency or speed-tuned inputs from outside MEC.

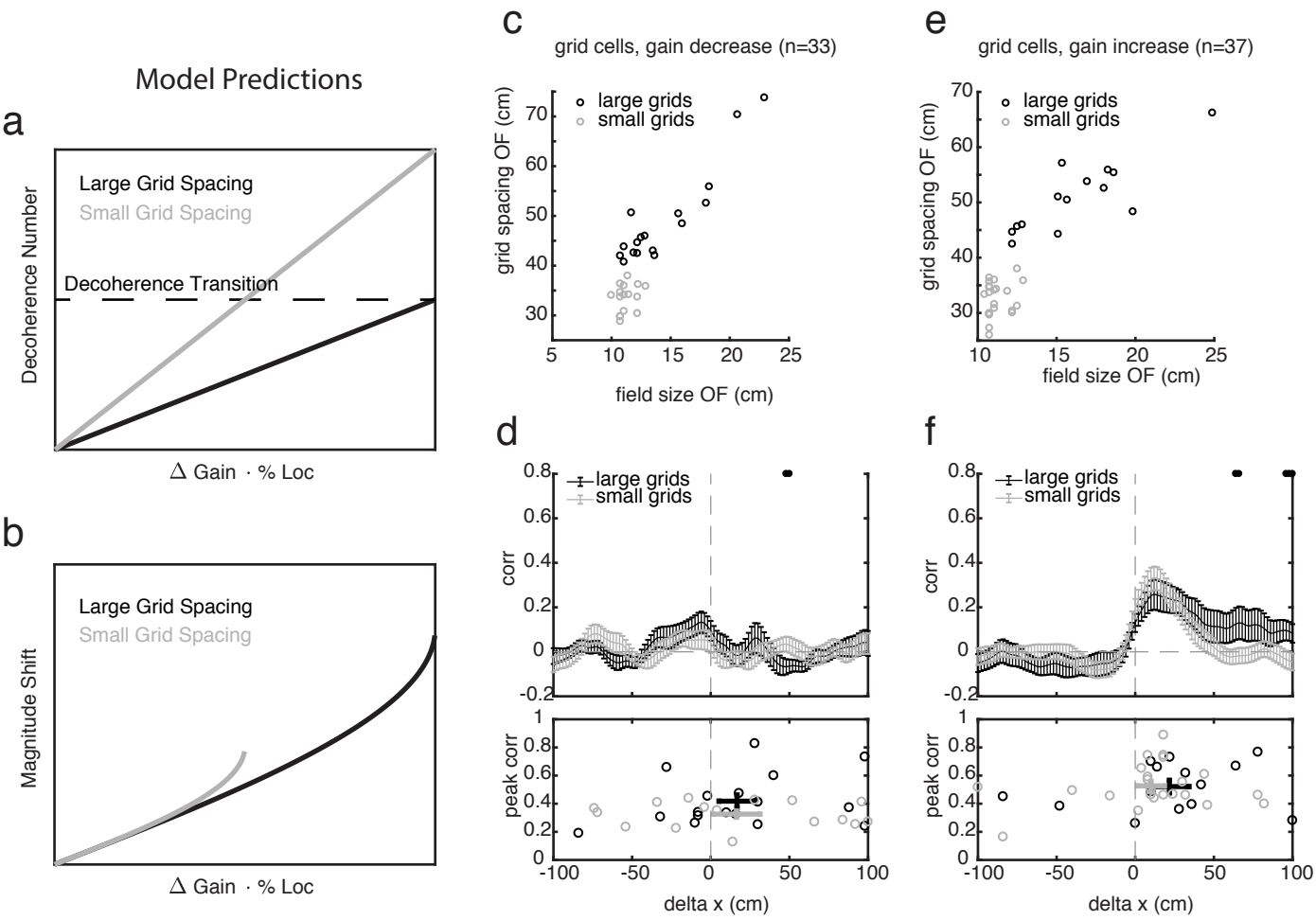
Model Predictions
a
Large Grid Spacing
Small Grid Spacing
Decoherence Transition
Decoherence Number
Δ Gain · % Loc
b
Large Grid Spacing
Small Grid Spacing
Magnitude Shift
Δ Gain · % Loc
c
grid cells, gain decrease (n=33)
large grids
small grids
grid spacing OF (cm)
field size OF (cm)
d
large grids
small grids
corr
peak corr
delta x (cm)
e
grid cells, gain increase (n=37)
large grids
small grids
grid spacing OF (cm)
field size OF (cm)
f
large grids
small grids
corr
peak corr
delta x (cm)

Supplementary Fig. 15: Grid scale does not strongly impact responses to gain manipulations. In the simulations in panels (a) and (b), "large" grid cells had spacing twice that of "small" grid cells; the exact value of the spacing is irrelevant. In the data panels (c-f), "large" grid cells were those with open field (OF) spacing > 40 cm and "small" grid cells were those with OF spacing <= 40 cm. **a)** The model predicts that at a given percent mismatch between path integration and landmarks, the decoherence number will be larger for small grid cells than large grid cells. Here, the "percent mismatch" is defined as $\Delta G \cdot \% Loc$, where ΔG is the change in gain and $\% Loc$ is the percent weighting of locomotor cues in the speed input (see also Fig. 6). This result predicts that small grid cells will decohere *before* large grid cells, i.e. at a less extreme gain value. However, since we only tested a small number of gains, we do not have the resolution to test this prediction in our dataset. **b)** Despite the difference in decoherence number, the shifts in grid cells will not depend on grid spacing in the sub-critical regime, to first order. This is because the larger decoherence number and smaller grid spacing cancel out (Supplementary Math Note, Part B). Therefore, the model predicts no difference in shifts during gain increase between small and large grid cells. The point where the lines end is where the pattern decoheres. This transition comes sooner for small grids than large grids, but within the sub-critical regime, the shifts are almost identical. **c)** OF field size vs. grid spacing for the 33 grid cells recorded on gain decreases. Large grids (n = 17) are shown in black and small grids (n = 16) are shown in gray. **d)** Top: Cross correlations of rate maps generated in the A and B periods of gain decreases for large grid cells (black) and small grid cells (gray). Black dots indicate bins where the two curves significantly differed at $p < 0.05$ (unpaired t-test, no correction for multiple comparisons). Bottom: Cross correlation peaks vs. the locations of these peaks. Neither the peak correlation nor the amount of shift significantly differed between large and small grid cells (peak correlation, mean ± SEM: large grids = 0.42 ± 0.04, small grids = 0.33 ± =0.02, Wilcoxon rank sum $p = 0.30$; shift, mean ± SEM: large grids = 16.7 ± 11.5 cm, small grids = 16.4 ± 15.0 cm, Wilcoxon rank sum $p = 0.86$). **e)** and **f)** Same as (c) and (d) but for gain increases (n = 14 large grid cells, 23 small grid cells). As predicted by the model, neither the peak correlation nor the amount of shift significantly differed between large and small grid cells (peak correlation, mean ± SEM: large grids = 0.52 ± 0.05, small grids = 0.53 ± 0.03, Wilcoxon rank sum $p = 0.89$; shift, mean ± SEM: large grids = 21.7 ± 12.6 cm, small grids = 10.0 ± 8.6 cm, Wilcoxon rank sum $p = 0.30$). Error bars: mean ± SEM.

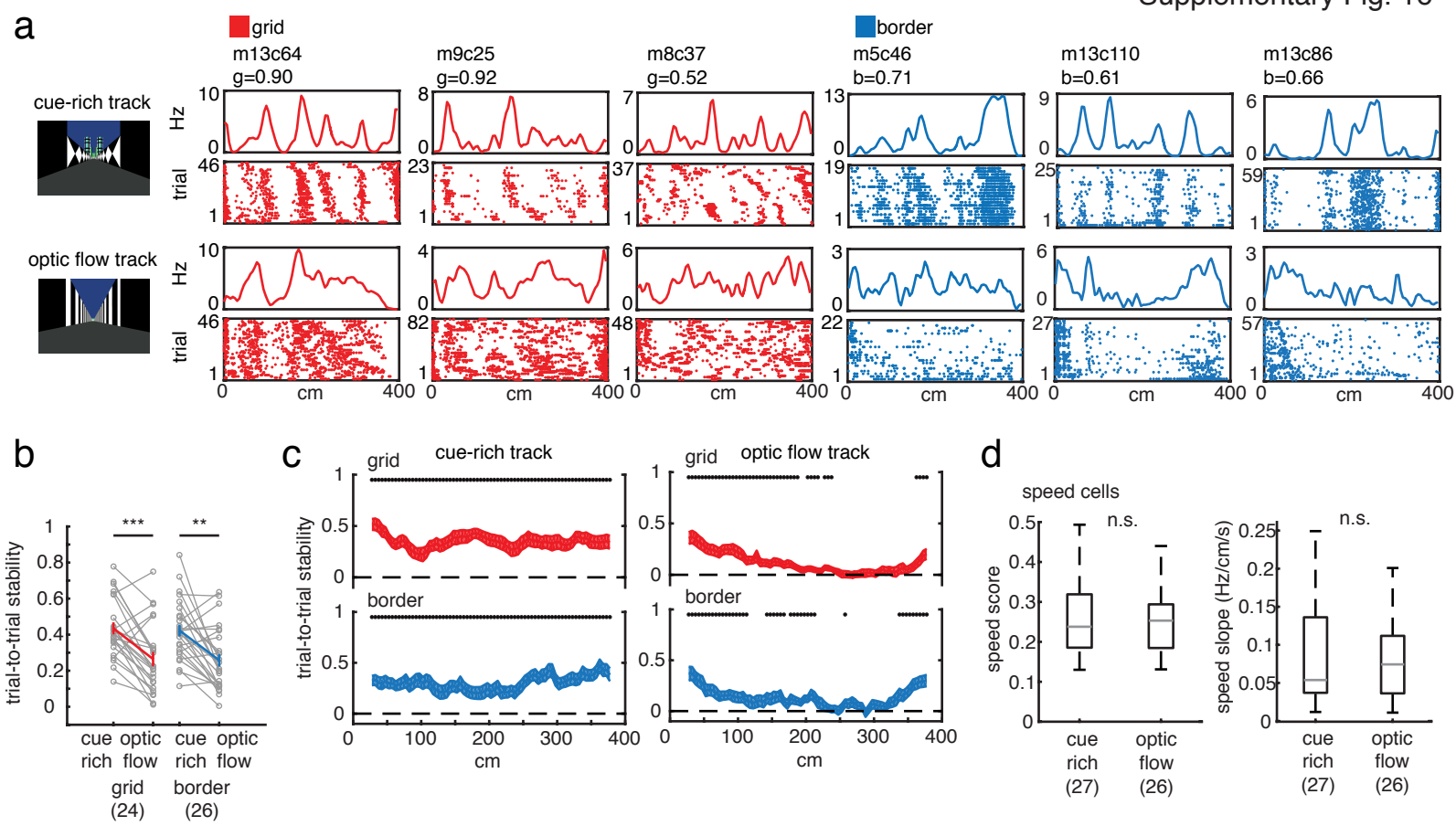

Supplementary Fig. 16: Grid cell stability decays after 200 cm in the absence of visual landmarks but presence of optic flow. **a)** Example responses to the cue-rich track (top) and optic flow track (bottom) (m=mouse number, c=cell number, g=grid score, b=border score). **b)** Trial-to-trial stability on the cue-rich track and optic flow track for grid and border cells (grid: n = 24, p = 0.00075; border: n = 26, p = 0.0012; Wilcoxon tests). **c)** Trial-to-trial stability vs. track location on the cue-rich track (left) and optic flow track (right). Black dots indicate significant non-zero trial-to-trial stability (t-test $p < 0.05$). **d)** Box and whisker plots of speed score (left) and speed slope (right) for speed cells identified on cue-rich track (n = 27) vs. optic flow track (n = 26) (speed score p = 0.95; speed slope p = 0.85; Wilcoxon rank-sum tests). Boxes show first and third quartiles, whiskers show maximum and minimum values, and gray lines indicate the median. n.s. not significant, ** $p < 0.01$, *** $p < 0.001$.

a

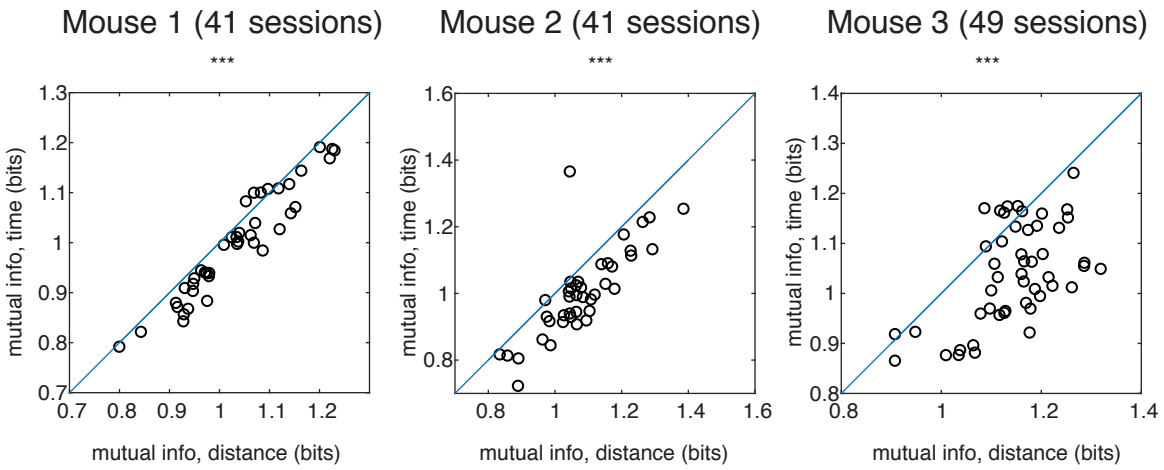

b

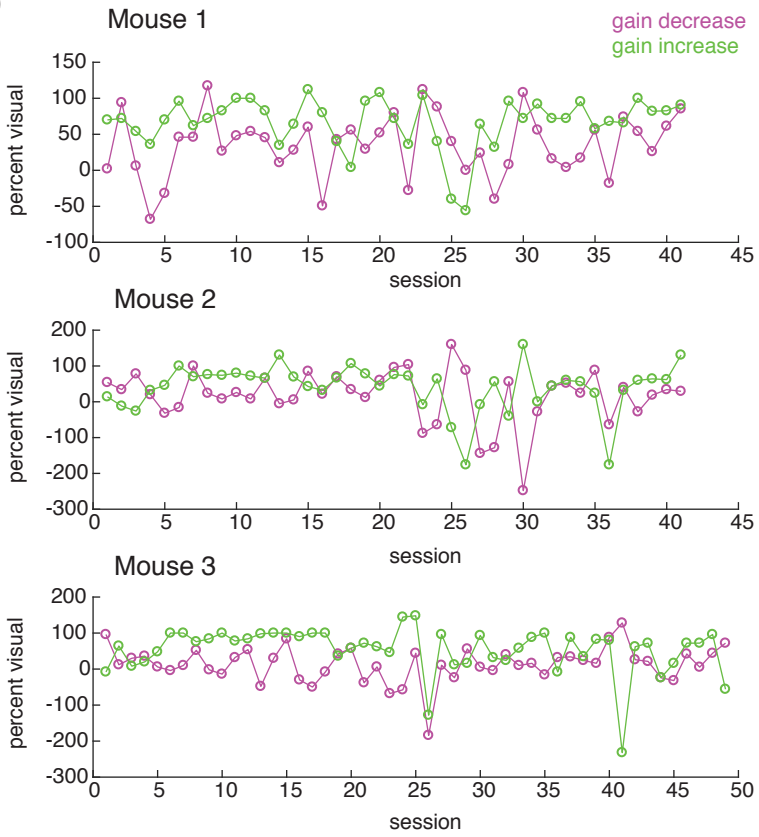

Supplementary Fig. 17: Additional behavioral task analyses. **a)** Mutual information was higher between running speed and distance than between running speed and time elapsed since the onset of the visual cues, demonstrating that the mice were integrating distance rather than time (mean mutual information with running speed ± SEM, mouse 1: distance = 1.03 ± 0.02, time = 1.00 ± 0.02, n = 41 sessions, Wilcoxon p = 3.9e-7; mouse 2: distance = 1.08 ± 0.02, time = 1.00 ± 0.02, n = 41 sessions, Wilcoxon p = 4.7e-7; mouse 3: distance = 1.15 ± 0.01, time = 1.04 ± 0.01, n = 49 sessions, Wilcoxon p = 3.9e-8; Online Methods). **b)** Percent weighting of visual cues did not change over sessions. This shows that no slow learning or sensitization process took place. *** $p < 0.001$.